Controlling Vertical Morphology within the Active Layer of Organic Photovoltaics Using Poly-(3-hexylthiophene) Nanowires and Phenyl-C_{61}-butyric Acid Methyl Ester

Andrew H. Rice,[†] Rajiv Giridharagopal,[‡] Sam X. Zheng,[†] Fumio S. Ohuchi,[†] David S. Ginger,[‡,*] and Christine K. Luscombe[†,*]

[†]Department of Materials Science and Engineering, University of Washington, Seattle, Washington 98195-2120, United States, and [‡]Department of Chemistry, University of Washington, Seattle, Washington 98195-1700, United States

ABSTRACT In this study, we demonstrate how the vertical morphology of bulk heterojunction solar cells, with an active layer consisting of self-assembled poly(3-hexylthiophene) (P3HT) nanowires and phenyl-C_{61}-butyric acid methyl ester (PCBM), can be beneficially influenced. Most device fabrication routes using similar materials employ an annealing step to influence active layer morphology, but this process can create an unfavorable phase migration where P3HT is driven toward the top of the active layer. In contrast, we demonstrate devices that exhibit an increase in relative fullerene concentration at the top of the active layer by introducing the donor phase as a solid nanowire in the active layer solution and altering the pre-spin drying time. X-ray photoelectron spectroscopy and conductive and photoconductive atomic force microscopy provide detailed images of how the surface of the active layer can be influenced; this is done by tracking the concentration and alignment of P3HT and PCBM domains. Using this new procedure, devices are made with power conversion efficiencies surpassing 2%. Additionally, we show that nanowires grown in the presence of the fullerene perform differently than those that are grown and mixed separately; exposure to the nanowire during self-assembly may allow the fullerene to coat nanowire surfaces and influence the photocurrent within the device.

KEYWORDS: P3HT nanowires · bulk heterojunction solar cells · conductive AFM · photoconductive AFM

Over the past decade, organic photovoltaics (OPVs) have emerged as a promising candidate for the generation of solar power. These devices are advantageous because their active layers can be made with solution processing onto flexible substrates. The potential for high-throughput, roll-to-roll processing could offer a dramatic reduction in processing costs of solar cells. Research in this field has largely focused on improving power conversion efficiencies (PCEs) of devices by either synthesizing new materials to improve band gap conditions/mobilities of materials[1−11] or increasing control over the device microstructure.[12−17] Here, we focus on new methods to control morphology using preformed poly(3-hexylthiophene) (P3HT) nanowires in classic bulk heterojunction (BHJ) structures with an active layer made up of the nanowires as the donor phase and phenyl-C_{61}-butyric acid methyl ester (PCBM) as the acceptor phase.

One of the simplest ways to affect the active layer structure of a device is through annealing. After active layer deposition, a heat treatment can cause the donor and acceptor phases to reorganize and form larger, more continuous domains. Once optimized, this process can dramatically improve both the microstructure and performance of BHJ devices.[18] However, in traditional BHJ cells, annealing can cause a potentially unfavorable vertical material gradient. The active layers of these devices are typically deposited on top of a poly(3,4-ethylene-dioxylene thiophene): poly(styrene sulfonic acid) (PEDOT:PSS) layer, which serves as a hole transport layer. In this scenario, annealing can produce an active layer with greater concentrations of PCBM toward the "bottom".[19,20] This segregation is attributed to differences in the surface energies of the components in the system. PCBM has a higher surface energy (37.8 mN/m^2) than P3HT (26.9 mN/m^2).[21] Therefore, more P3HT ends up at the air:active layer interface, while PCBM becomes concentrated downward. However, the effect of annealing on vertical phase separation is currently under debate; a few recent studies have argued that annealing can produce beneficial increases in the PCBM concentration at the top of the active layer.[22,23]

* Address correspondence to luscombe@u.washington.edu or ginger@chem.washington.edu.

Received for review January 21, 2011 and accepted March 28, 2011.

Published online March 28, 2011
10.1021/nn2002695

In principle, one would prefer higher concentrations of the electron-accepting species at the "top" of the active layer because such a configuration would aid in electron transport to the top electrode and block hole transport to the top surface. Therefore, the material gradient that the majority of research groups have observed in most P3HT/PCBM systems is unfavorable and may lower the efficiency of the system.

In this paper, we present an alternative approach to controlling vertical morphology by using a combination of P3HT nanowires and PCBM in the active layer of devices. Using this system, it is possible to manufacture devices with increased PCBM concentration at the top of the active layer. The ability to influence and control the vertical concentration gradient of PCBM and P3HT in the active layer provides a useful tool for optimizing the microstructure and increasing the PCE of OPVs.

RESULTS AND DISCUSSION

OPVs were made using P3HT nanowires and PCBM as the active layer components. Device fabrication followed a route similar to the whisker method[24] (see Methods section), but included an extra processing step to increase active layer thickness. This additional step, referred to here as "pre-spin drying time", is a period of time between the initial application of the active layer solution to substrate and the time when spin-coating is initiated. During this period, the solvent in the solution evaporates, increasing the viscosity of the active layer solution, which should lead to a thicker film upon spin-coating. This processing step will be discussed in greater detail later in the paper.

In order to increase control over the active layer morphology of the device, it may be important to understand the effect that PCBM has on P3HT nanowire formation and growth. This effect was investigated by processing films under two different conditions: process A (where PCBM is added to solution before nanowire self-assembly) and process B (where PCBM is added to solution after nanowire self-assembly). Films were made using both of these processes and were characterized and compared to one another. In process A, PCBM has the potential to directly affect nanowire formation; this is not the case in process B. By comparing films made from these two solutions, it may be possible to gain insight into how PCBM affects P3HT nanowires.

OPVs were made using processes A and B, and their photovoltaic performance was compared (Figure 1). Figure 1 illustrates the effect of the processing condition on photovoltaic properties. The overall trend for device performance is the same in each scenario: efficiencies increase steadily with longer pre-spin drying time. However, the devices made when the PCBM was added after the nanowires had already formed were less than half as efficient as devices where the PCBM was in the solution during nanowire formation. Figure 2 provides representative $J-V$ curves for processes A and B, showing a direct comparison between the two processing conditions.

We hypothesize that introducing the PCBM after nanowire formation, as opposed to before, may alter how P3HT and PCBM interact in the active layer. One could speculate that the PCBM may be incorporated into the nanowire structure or could coat the nanowire surfaces during their formation. However, neither possibility seems to be supported by the experimental data available. Using X-ray diffraction (XRD) (Figure S1), we see no difference between spectra for the P3HT nanowires regardless of whether they are formed in the presence of PCBM or not, suggesting either that any interaction between the PCBM and the nanowires during their formation is along a crystallographic axis not observed in our XRD data (e.g., (010) or (001)) or that the PCBM/P3HT interaction occurs at the surface of the nanowires.[25−27] Additionally, we found the diameters of the nanowires to be the same to within experimental error (Figure 3), regardless of whether PCBM was present during nanowire formation or not, arguing against a coating of PCBM forming around the wires. Varying the pre-spin drying time for each of the processes (between 0 and 5 min) also failed to significantly alter the average nanowire height.

To study the effect of processing on the devices, we used conductive atomic force microscopy (cAFM) and photoconductive atomic force microscopy (pcAFM) to image the current transport networks in these devices, in order to better understand the changes in performance at the local level. In these experiments, we used cAFM to probe the dark current and pcAFM to probe the short-circuit photocurrent (see Methods section). In both techniques, the conducting gold tip forms the top contact of a nanoscale solar cell.[29,30] For these systems, it is expected that in the forward-biased case (where the tip is biased positive, relative to the sample) we observe hole transport images, while for the reverse-biased case we observe electron transport.[31] Electron injection is possible despite the large barrier at the Au/organic interface in part because the high electric field concentration at the sharp AFM tip facilitates injection. In these images, we expect that the dark hole current will be largest where there are well-connected P3HT nanowire pathways from the top surface to the bottom contact; similarly, we would expect dark electron currents to be largest in areas where there are well-connected PCBM pathways from the top to the bottom. Alternatively, the short-circuit photocurrent images indicate areas where both photogenerated electrons and photogenerated holes can be extracted efficiently through the contacts. We have generated comparable data in previous studies of nanowire-based solar cells.[32]

In addition to analyzing devices with new active layer morphologies, the other critical difference between this investigation and older studies is that we successfully

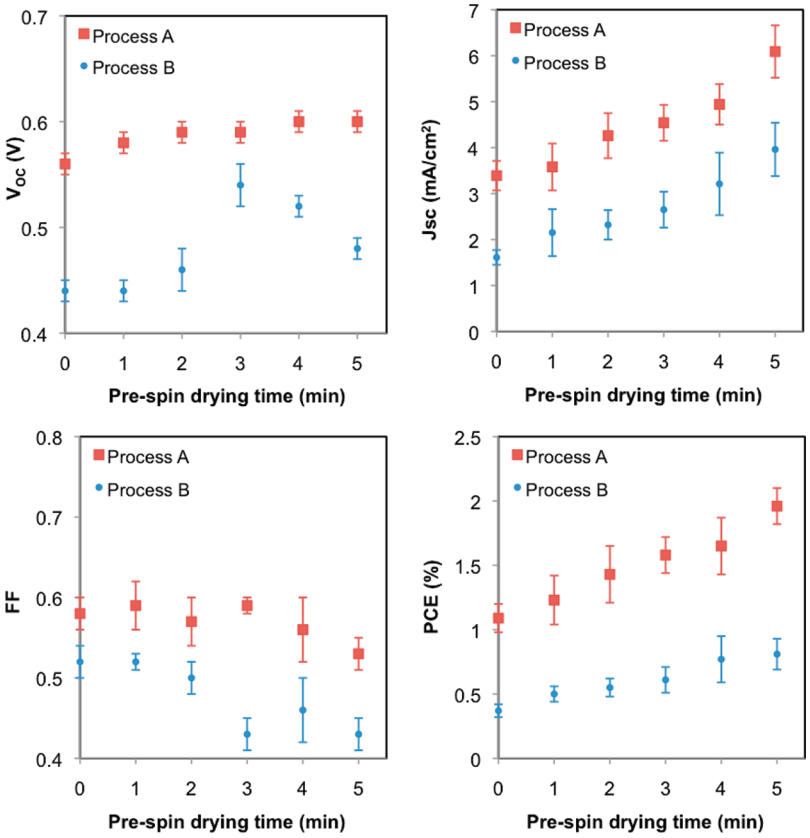

Figure 1. Effect of pre-spin drying time on device performance for processes A (PCBM added before nanowire assembly) and B (PCBM added after nanowire assembly). At least 24 devices were tested and averaged under each set of processing conditions. Error bars represent one standard deviation from the mean.

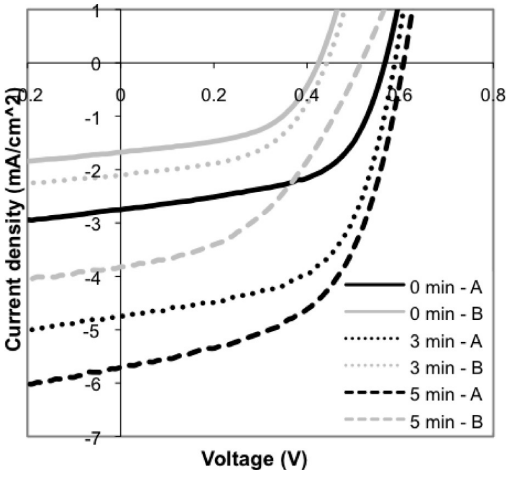

Figure 2. Effect of pre-spin drying time (0, 3, and 5 min) and processing condition (A, process A; B, process B) on device performance.

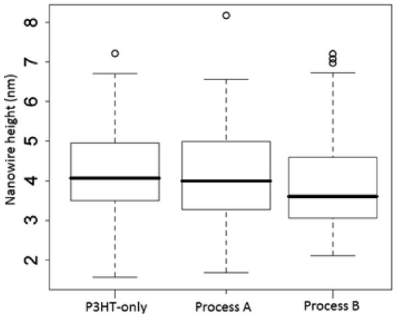

Figure 3. Box and whisker plot showing the effect of processing condition on nanowire height. Process A is where the PCBM is added during nanowire formation. Process B is where the PCBM is added to solution after nanowire formation. The nanowire thicknesses appear identical within experimental error, while a PCBM monolayer would be expected to be around 1 nm thick.[28]

imaged these new films in attractive contact mode, so that we are able to correlate the dark hole, electron, and short-circuit photocurrent over the *same* region of the device with minimal film damage (see Figure S2). Using cAFM and pcAFM we are able to observe how the two different processes affect local electronic behavior in terms of PCBM–nanowire interaction. Figure 4 shows sets of data taken with the same tip for films made with the PCBM added during nanowire formation (process A, Figure 4A–D) or added after nanowire formation (process B, Figure 4E–H). We made sure to use the same approximate laser intensity to avoid intensity-dependent photocurrent effects.[33] Topographically, the two films are similar in that we observe nanowires of comparable dimensions and density.

The spatially averaged dark hole current increases significantly when the PCBM is added after nanowire

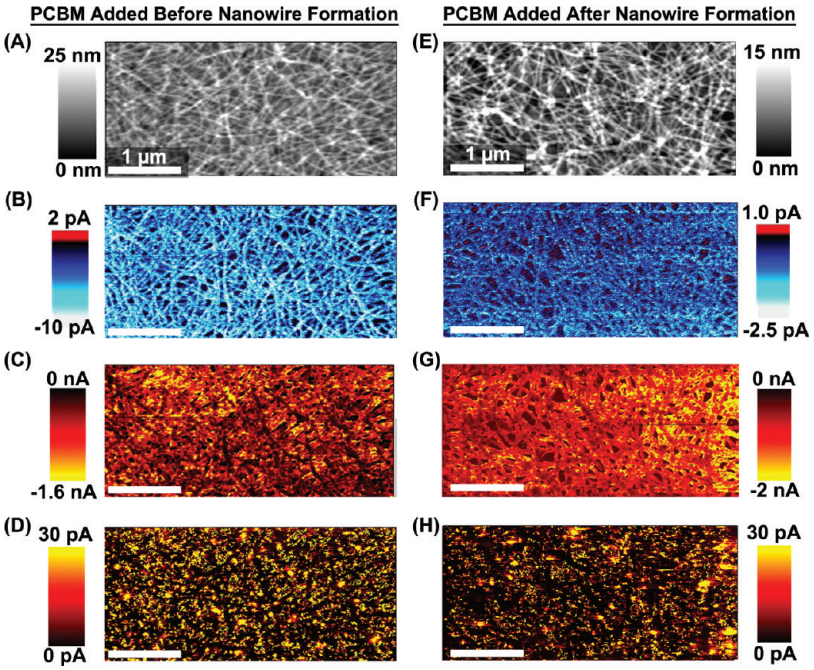

Figure 4. Correlated (A) topography, (B) short-circuit photocurrent, (C) dark hole current (+3 V applied to the tip), and (D) dark electron current (−3 V applied to the tip) on a film made with process A, where the PCBM is added during nanowire formation. (E−H) The same correlated images for a film made with process B, where the PCBM is added to the solution after the nanowires have formed. The same AFM tip was used and the laser intensity held constant for both sets of data.

formation (process B). For the process A film in Figure 4C, the average dark hole current is −488 pA, while the process B film exhibits an average dark hole current of −622 pA in Figure 4G. The spatially averaged dark electron current shows the opposite trend. In Figure 4D, the process A film has an average dark electron current of 25 pA, while the process B film in Figure 4H has an average dark electron current of 11.7 pA. The pcAFM data measure higher photocurrents in the film made with process A, in good agreement with the macroscopic device results. The average photocurrent decreases from *ca.* −5.0 pA to *ca.* −1.0 pA when using process B instead of A. The areas of efficient dark transport are not obviously correlated with areas of high photocurrent, similar to that observed for P3HT-PCBM films.[31] The isolated regions of dark electron current in Figure 4D and H do not appear to be caused by topographic effects such as the tip pulling on the fibers, as that would cause noticeable film damage and, most likely, significant change in the associated short-circuit photocurrent images (see Figure S2).

These three sets of current data are consistent with the hypothesis that adding the PCBM after nanowire formation (process B) negatively alters the film morphology, possibly through changes in the PCBM−nanowire interaction that inhibit intimate coating of the nanowires. Our photocurrent data are consistent with this interpretation, given the 5× increase in average photocurrent for process A versus process B. A more intimate PCBM coating as in process A might be expected to enhance exciton dissociation at the nanowires and increase the average photocurrent, even though the photocurrent is negative in both films. We interpret the changes in dark current averages to changes in relative PCBM surface concentration and nanowire connectivity. The higher dark electron current in process A implies higher PCBM surface concentration; the higher dark hole current in process B, on the other hand, indicates higher nanowire coverage at the surface and better connectivity to the bottom electrode. The higher electron current and lower hole current in process A are therefore indicative of a preferential morphology for device performance, confirmed through the short-circuit photocurrent data and device measurements in Figures 1 and 2. The dark current and photocurrent data are self-consistent in terms of the trends exhibited by the change in processing.

In addition to observing the effect of PCBM on P3HT nanowire growth, we also further investigated the effects of pre-spin drying time on device morphology and performance. The photovoltaic results for pre-spin drying times up to 5 min are shown in Figure 5; at least 24 devices were tested under each set of processing conditions. Devices used in this study were made using process A because this fabrication route produced higher performance solar cells as discussed earlier (Figure 2). Devices were also made with longer pre-spin drying times, but the viscosity of the active layer solution increased to the point where consistently good films could no longer be made *via* spin-coating. Device performance peaked at a pre-spin drying time of 5 min.

The data in this figure demonstrate that for increasing pre-spin drying times both the J_{SC} and the PCE steadily

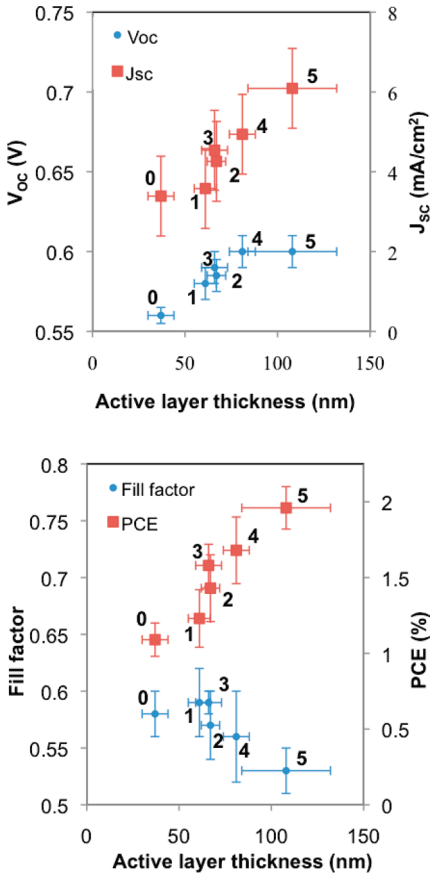

Figure 5. Device parameters plotted as a function of active layer thickness. The numbers next to data points represent the pre-spin drying time in minutes. Devices were fabricated using process A. Error bars represent one standard deviation from the mean.

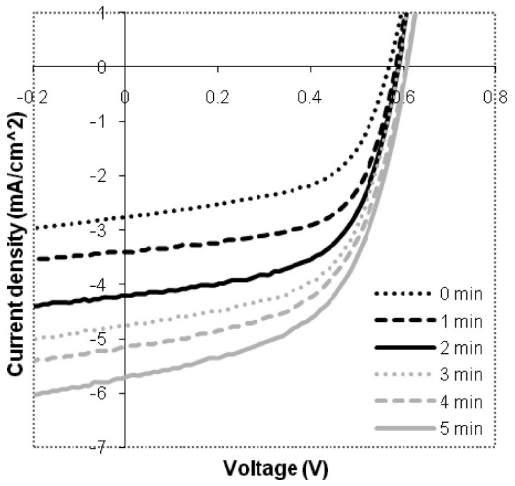

Figure 6. Current–voltage curves for devices made with different pre-spin drying times showing the effect of pre-spin drying time on device performance. The 1, 2, and 3 min devices had similar active layer thicknesses, so performance differences between these three may be due to changes in active layer morphology.

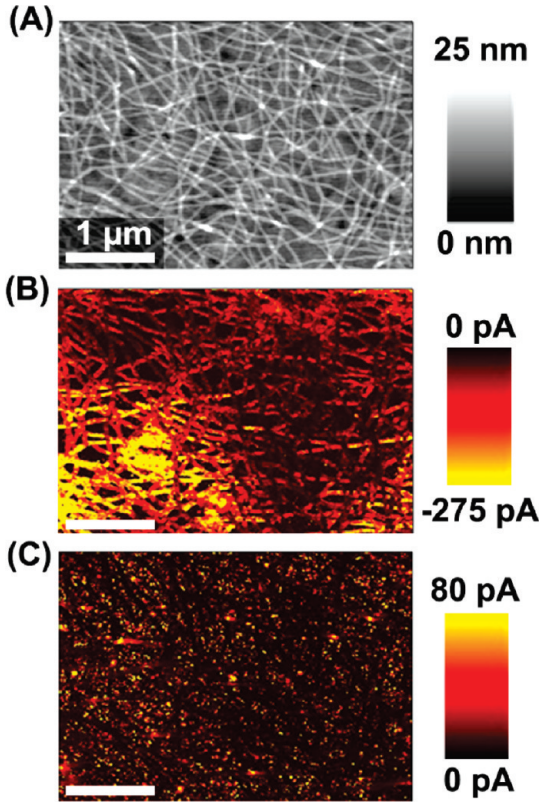

Figure 7. Correlated (A) topography, (B) dark hole current (+3 V applied to the tip), and (C) dark electron current (−3 V applied to the tip) on a P3HT nanowire:PCBM film with no pre-spin drying time.

increase while the V_{OC} remains fairly constant and the fill factor decreases. The rise in J_{SC} is likely related to the increase in absorption brought about by a thicker active layer, which could lead to a more efficient device. The reduction in fill factor may be caused by the decrease in the shunt resistance of the devices as the pre-spin drying time increases. A lower shunt resistance indicates lower charge extraction efficiency; however, as the absorption of our active layer increases, we should be able to generate significantly more charges, so we still observe an overall increase in device efficiency.

It should be noted that the active layer thickness does not steadily increase with increased pre-spin drying times. Between 1 and 3 min, the active layer thickness remains fairly constant. Improvement in device performance without increased active layer thickness suggests that other factors may be influencing device efficiency. Figure 6 shows representative *J*–*V* curves from these devices, graphically illustrating the increase in device performance with longer pre-spin drying times.

We hypothesize that an increase in pre-spin drying time allows the P3HT and PCBM in the active layer to rearrange and adopt an altered distribution, impacting the microstructure of the device. To test this theory, we used cAFM to image the change in current behavior as a function of pre-spin drying time. Figures 7A–C and 8A–C show the topography and correlated dark hole and electron current for the film formed with no pre-spin

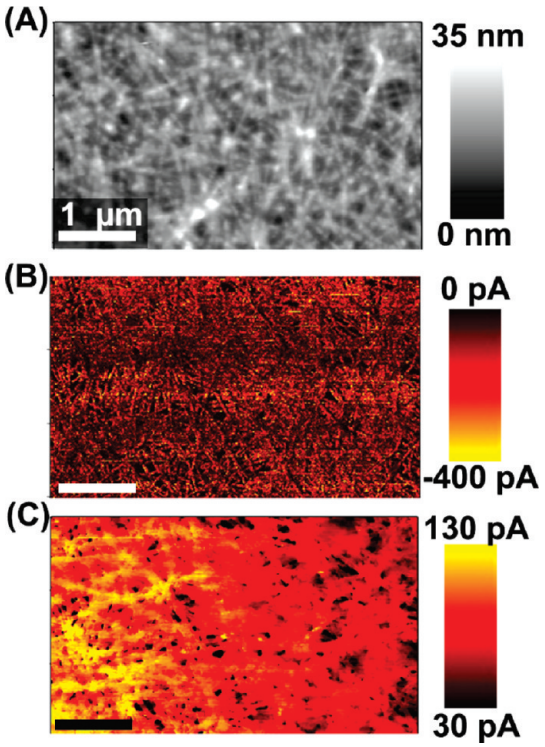

Figure 8. Correlated (A) topography, (B) dark hole current (+3 V applied to the tip), and (C) dark electron current (−3 V applied to the tip) on a P3HT nanowire:PCBM film with 5 min pre-spin drying time.

drying time (Figure 7) and with a 5 min pre-spin drying time step (Figure 8). These conditions correspond to total film thicknesses of ∼37 and ∼108 nm, shown in Figure 5. The sets of data were taken with the same tip to avoid undue influence from different tip states. We observe two key features in these data. First, the dark electron current in the 0 min film is significantly less than that in the 5 min film, *despite the fact that the 0 min film is thinner*. The average of the dark electron current is ∼9 pA in the 0 min film yet is ∼81 pA in the 5 min film. Furthermore, the electron transport image in Figure 8C (5 min film) has a nonzero current background as opposed to the isolated hot spots of transport amidst a largely zero current background seen in Figure 7C for the zero drying time film (see Figure S3 for histogram data). Second, in terms of dark hole current, we observe areas of "hot" nanowires in the 0 min film (lower left, Figure 7B) where the hole current reaches values as high as −1.34 nA, with an average current of −55 pA. The image of the film spin-coated with a 5 min pre-spin drying time in Figure 8B shows that the average hole current has increased to −77 pA, consistent with the expectations of better P3HT ordering, although the change for holes (∼1.4× increase) is significantly smaller than the change observed for electron transport (∼9× increase).

We interpret both the 9-fold increase in electron dark current with pre-spin drying time and the concomitant transition of the local spatial distribution of electron transport from being "mostly off" in Figure 7C to "mostly on" in Figure 8C as being associated with both an increase in PCBM connectivity in the film and a significant change in the fraction of PCBM that is exposed (or very near) to the top film/air interface, allowing electrons to be injected from the cAFM tip into the PCBM domains. In this picture, the electron transport hotspots in Figure 7C would be consistent with small numbers of PCBM domains that penetrate the P3HT wetting layer on the film surface,[30] while the more uniform electron currents in Figure 8C would correspond to a much larger number of exposed or near-surface PCBM domains. That is, we are able to infer from these cAFM data that important changes in both the connectivity and top surface concentration of PCBM are occurring due to the pre-spin drying step.

While the cAFM data are suggestive, the X-ray photoelectron spectroscopy (XPS) data provide clear spectroscopic evidence for this hypothesis. XPS can be used to monitor changes in surface composition in P3HT/PCBM blends by comparing the signature peaks for oxygen-1s (O1s) and sulfur-2p (S2p).[34] The concentration of P3HT scales with the S2p peak, while the concentration of PCBM correlates to the intensity of the O1s peak. The spectra for these two peaks collected from devices with different pre-spin drying times are displayed in Figure 9. Care was taken to ensure that the films were not exposed to air to limit contamination from ambient oxygen. All peaks have been normalized to the signature C1s peak.

These graphs shows that the O1s peak intensity increases and the S2p peak decreases with longer pre-spin drying times, indicating that the P3HT concentration at the film/air interface is decreasing (and the PCBM concentration is increasing) with increasing pre-spin drying time. Attempts to delaminate our films in order to perform XPS on the "bottom" of the active layer, to see if a complementary change in concentration is evident at the film/PEDOT interface, proved to be unsuccessful due to the relatively low thicknesses of many of our films (25−100 nm). However, because the trends observed in Figure 9 support our cAFM data, we believe that the observed changes in concentrations are meaningful.

Evidently, changing the length of the pre-spin drying time strongly alters the material gradient in the active layer, providing greater control over the vertical morphology. These changes in vertical morphology have important implications for device optimization. In standard BHJ device architectures, higher concentrations of the electron-accepting species at the top of the active layer should be preferred because this would aid in electron transport to the top electrode. Therefore, the material gradient that is generated with increased pre-spin drying times should be more favorable, and may contribute to the improved performance we observe in our devices with increasing pre-spin drying times.

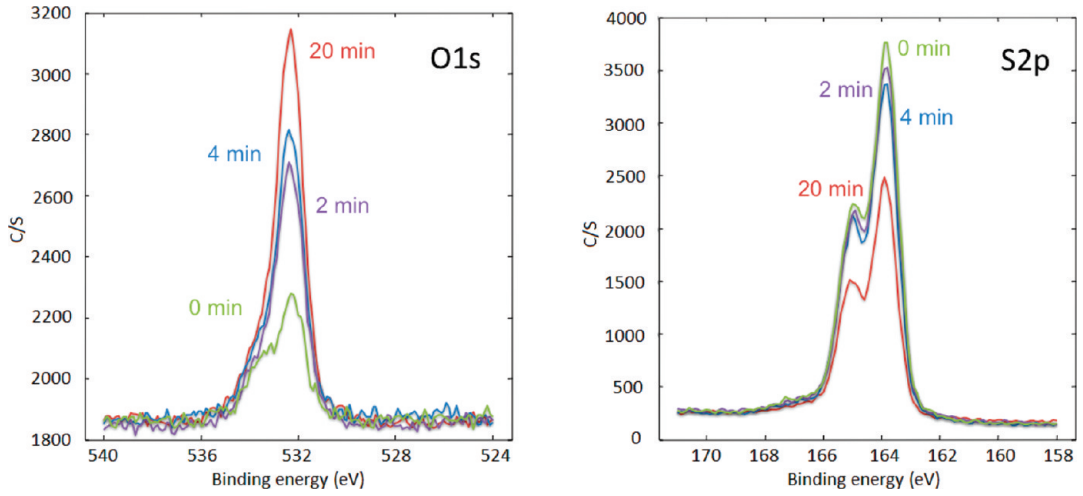

Figure 9. XPS spectra (45-degree resolve) of film surfaces at different pre-spin drying times corresponding to the presence of O1s PCBM and S2p P3HT.

We next discuss possible explanations for the radically different vertical morphology observed in these experiments as compared to P3HT/PCBM blend films without preformed P3HT nanowires. It is possible such behavior could arise if P3HT nanowire films exhibit a significantly different surface energy than normal P3HT films. However, contact angle measurements, corrected for the effects of surface roughness using Wenzel's equation,[35] show that P3HT films containing nanowires and those without nanowires have similar surface energies. Thus, we conclude that the differences in vertical morphology of the P3HT nanowire films must have another explanation.

An alternative hypothesis to explain the phase separation is that the P3HT nanowires are simply settling out of solution during the pre-spin drying time. Unlike traditional active layer solutions, where both the P3HT and PCBM phases are dissolved in solution, the P3HT nanowires are insoluble at room temperature, forming solid particles. Over time, gravity causes these nanowires to sink, leading to an increase in P3HT concentration at the bottom of the vial. If this phenomenon occurs on the substrate during the pre-spin drying time, this would leave behind a PCBM-rich region toward the top of the active layer. Upon spin-coating, this phase separation is effectively frozen within the active layer microstructure, causing the phase segregation that we noticed above.

It was observed that when left at rest in a vial, it took days for the nanowires to noticeably settle out of solution. In this scenario, the volume of solution was 1−2 mL and settling occurred over a distance of >1 cm. However, when the active layer solution is deposited on the device substrate, a much smaller volume is used (60 μL) and the settling distance is much smaller (~0.03 cm). Smaller volumes and shorter settling distances significantly increase the observed sedimentation rate of a suspension. Therefore, it does not seem unrealistic that a noticeable change in P3HT concentration could occur during pre-spin drying times of less than 5 min.

A final hypothesis is that the pre-spin drying time allows for the formation of larger PCBM crystals, which support better connectivity and are more likely to penetrate the top film surface and contribute to the O-1s signal in the XPS measurements.

CONCLUSION

We have successfully demonstrated a processing technique based on preformation of P3HT nanowires that can be used to control vertical composition gradients within the active layer of bulk heterojunction solar cells. By using P3HT nanowires and introducing a "pre-spin drying time" step, we are able to increase the amount of PCBM at the top of the active layer. This provides greater control over the device microstructure and can be used to produce more efficient OPVs. Additionally, we showed that PCBM influences the efficiency of P3HT nanowires in OPVs. While the mechanism remains unclear, the presence of PCBM during nanowire formation greatly influences device performance and microstructure and thereby improves device efficiencies; this knowledge represents another tool that could be utilized to create more efficient OPVs.

METHODS

Fabrication. The substrates used in this study were ITO-coated glass (15 Ω/m^2, supplied by Colorado Concept Coatings) cut into 1.5 × 1.5 cm squares. Substrates were cleaned *via* a series of ultrasonic baths in a mild detergent, deionized water, acetone, and isopropyl alcohol. The substrates were removed from the last bath and dried using N_2. They were then treated with air plasma for 10 min under vacuum (200 mTorr).

Once clean, substrates were coated with filtered PEDOT:PSS (Clevios PVP Al 4083). The PEDOT:PSS was spin-coated, in air, on top of the ITO surface from solution to obtain a layer roughly 40 nm thick. These films were annealed in air at 140 °C for 10 min. They were then stored under argon until the active layer was prepared.

Active layer preparation began by making the solvent, which was comprised of 80 vol % anisole combined with 20 vol % chloroform. P3HT (Rieke Metal, Sepiolid P100) and PCBM (American Dye Source Inc. ADS61BFB) were added to the solvent, and the solution was stirred in the dark inside the glovebox at 500 rpm for 3 h at 70 °C. The ratio between P3HT:PCBM was maintained at 1:0.8 (by weight). After 3 h, the solution was removed from heat and stored in the dark overnight (~18 h) to allow the nanowires to self-assemble in solution. The solution was then deposited on top of the PEDOT:PSS layer. At this point, the appropriate pre-spin drying time was allowed. Deposition was completed by spin-coating at 1000 rpm for 60 s. Finally, electrodes were deposited on top of the active layer *via* thermal evaporation. A 1 nm layer of LiF followed by a 100 nm layer of Al were evaporated under vacuum (2×10^{-6} Torr) to form the electrodes.

Characterization. The *J*−*V* characteristics of the resultant devices were immediately tested after processing was completed. This was done in air using a Keithley 2400 source measurement unit and an Oriel Xenon lamp (450 W). An AM 1.5 filter was used as the light source. Calibration of the light intensity was completed using a standard silicon solar cell with a KG5 filter. A light intensity of 100 mW·cm^{-2} was used throughout this study. The series resistance and parallel resistance were calculated from the inverse of the slope of the *J*−*V* curve at 1 and 0 V, respectively. At least 24 devices were tested and averaged during *J*−*V* characterization. It should be noted that the objective of this work is to demonstrate trends in the data between different processes, not to produce champion data. For this reason, the spectral mismatch factor was not included in the measurements.

XPS spectra were generated using a PHI Versaprobe system with an Al Kα X-ray source and a 1 μm beam size. Measurements were taken while the sample was under ultrahigh vacuum (10^{-10} Torr).

Imaging. Tapping mode AFM images were taken on a Veeco multimode AFM with a Nanoscope III controller in tapping mode. The AFM tips used for this study were purchased from Veeco: model RTESP ($f \approx 300$ kHz, $k \approx 40$ N/m) phosphorus doped-Si tips. Active layer thicknesses were measured using the scratch test.

Conductive and photoconductive AFM images were acquired using an atomic force microscope (MFP-3D-BIO, Asylum Research) mounted on an inverted optical microscope (Nikon Eclipse TE2000-U). Images were acquired using gold-coated silicon cantilevers (CONTE-GB, $k \approx 0.2$ N/m, Budget Sensors). Because of the soft nature of these samples, the samples were imaged in attractive contact mode rather than the typical repulsive-regime contact mode. All samples were mounted in a sealed fluid cell inside an oxygen/water-free glovebox and imaged under constant nitrogen flow to protect against photo-oxidation. For photoconductive AFM, a 532 nm laser (Crystal Laser GCL-005 L, 5 mW) was focused at the top of the sample, attenuated with neutral density filters, and coaligned with the apex of the tip. Therefore, the images acquired represent the short-circuit photocurrent. The laser intensity was kept constant between images using an adjustable neutral density filter and sampled at approximately 10^8 W/m^2. Currents observed here are lower than observed in previous polythiophene nanowire work;[32] we tentatively attribute this to the lack of tip penetration due to attractive imaging, therefore limiting the contact area. We did not notice any significant change in photocurrent with intensity; however, because photocurrents seem to be lower in the attractive contact method, we have a limited range of possible laser intensities. Attractive-mode pcAFM is highly sensitive to imaging conditions and feedback settings, and instability in the imaging parameters can cause the tip to drift out of contact with the surface. This effect is amplified if imaging occurs within the first 30 min of approaching, possibly due to piezo hysteresis.

Acknowledgment. This work was made possible by grants from the National Science Foundation (DMR-0120967 and the NSF CAREER Award DMR-0747489). The authors thank O. G. Reid for helpful discussions regarding pcAFM imaging.

Supporting Information Available: Additional information discussing X-ray diffraction data, photoconductive/conducting atomic force microscopy (pcAFM/cAFM) data, and comments regarding the differences between "repulsive" and "attractive" mode imaging is available free of charge *via* the Internet at http://pubs.acs.org.

REFERENCES AND NOTES

1. Muhlbacher, D. S., M.; Morana, M.; Zhu, Z. G.; Waller, D.; Gaudiana, R.; Brabec, C. High Photovoltaic Performance of a Low-Bandgap Polymer. *Adv. Mater.* **2006,** *18*, 2884–2889.
2. Thompson, B. C.; Kim, Y. G.; McCarley, T. D.; Reynolds, J. R. Soluble Narrow Band Gap and Blue Propylenedioxythiophene-Cyanovinylene Polymers as Multifunctional Materials for Photovoltaic and Electrochromic Applications. *J. Am. Chem. Soc.* **2006,** *128*, 12714–12725.
3. Wong, W. Y.; Wang, X. Z.; He, Z.; Chan, K. K.; Djurisic, A. B.; Cheung, K. Y.; Yip, C. T.; Ng, A. M. C.; Xi, Y. Y.; Mak, C. S. K.; *et al.* Tuning the Absorption, Charge Transport Properties, and Solar Cell Efficiency with the Number of Thienyl Rings in Platinum-Containing Poly(Aryleneethynylene)s. *J. Am. Chem. Soc.* **2007,** *129*, 14372–14380.
4. Blouin, N.; Michaud, A.; Gendron, D.; Wakim, S.; Blair, E.; Neagu-Plesu, R.; Belletete, M.; Durocher, G.; Tao, Y.; Leclerc, M. Toward a Rational Design of Poly(2,7-Carbazole) Derivatives for Solar Cells. *J. Am. Chem. Soc.* **2008,** *130*, 732–742.
5. Chen, C. P.; Chan, S. H.; Chao, T. C.; Ting, C.; Ko, B. T. Low-Bandgap Poly(Thiophene-Phenylene-Thiophene) Derivatives with Broaden Absorption Spectra for Use in High-Performance Bulk-Heterojunction Polymer Solar Cells. *J. Am. Chem. Soc.* **2008,** *130*, 12828–12833.
6. Hou, J. H.; Chen, H. Y.; Zhang, S. Q.; Li, G.; Yang, Y. Synthesis, Characterization, and Photovoltaic Properties of a Low Band Gap Polymer Based on Silole-Containing Polythiophenes and 2,1,3-Benzothiadiazole. *J. Am. Chem. Soc.* **2008,** *130*, 16144–16145.
7. Wang, E. G.; Wang, L.; Lan, L. F.; Luo, C.; Zhuang, W. L.; Peng, J. B.; Cao, Y. High-Performance Polymer Heterojunction Solar Cells of a Polysilafluorene Derivative. *Appl. Phys. Lett.* **2008,** *92*, 033307.
8. Wienk, M. M.; Turbiez, M.; Gilot, J.; Janssen, R. A. J. Narrow-Bandgap Diketo-Pyrrolo-Pyrrole Polymer Solar Cells: The Effect of Processing on the Performance. *Adv. Mater.* **2008,** *20*, 2556–2560.
9. Chen, H. Y.; Hou, J. H.; Zhang, S. Q.; Liang, Y. Y.; Yang, G. W.; Yang, Y.; Yu, L. P.; Wu, Y.; Li, G. Polymer Solar Cells with Enhanced Open-Circuit Voltage and Efficiency. *Nat. Photonics* **2009,** *3*, 649–653.
10. Park, S. H.; Roy, A.; Beaupre, S.; Cho, S.; Coates, N.; Moon, J. S.; Moses, D.; Leclerc, M.; Lee, K.; Heeger, A. J. Bulk Heterojunction Solar Cells with Internal Quantum Efficiency Approaching 100%. *Nat. Photonics* **2009,** *3*, 297–302.
11. Qin, R. P.; Li, W. W.; Li, C. H.; Du, C.; Veit, C.; Schleiermacher, H. F.; Andersson, M.; Bo, Z. S.; Liu, Z. P.; Inganäs, O.; *et al.* A Planar Copolymer for High Efficiency Polymer Solar Cells. *J. Am. Chem. Soc.* **2009,** *131*, 14612–14613.
12. Coakley, K. M.; McGehee, M. D. Conjugated Polymer Photovoltaic Cells. *Chem. Mater.* **2004,** *16*, 4533–4542.
13. Blom, P. W. M.; Mihailetchi, V. D.; Koster, L. J. A.; Markov, D. E. Device Physics of Polymer: Fullerene Bulk Heterojunction Solar Cells. *Adv. Mater.* **2007,** *19*, 1551–1566.
14. Thompson, B. C.; Frechet, J. M. J. Organic Photovoltaics—Polymer-Fullerene Composite Solar Cells. *Angew. Chem., Int. Ed.* **2008,** *47*, 58–77.
15. Gunes, S.; Neugebauer, H.; Sariciftci, N. S. Conjugated Polymer-Based Organic Solar Cells. *Chem. Rev.* **2007,** *107*, 1324–1338.

16. Giridharagopal, R.; Ginger, D. S. Characterizing Morphology in Bulk Heterojunction Organic Photovoltaic Systems. *J. Phys. Chem Lett.* **2010,** *1*, 1160–1169.
17. Groves, C.; Reid, O. G.; Ginger, D. S. Heterogeneity in Polymer Solar Cells: Local Morphology and Performance in Organic Photovoltaics Studied with Scanning Probe Microscopy. *Acc. Chem. Res.* **2010,** *43*, 612–620.
18. Huang, Y. C.; Liao, Y. C.; Li, S. S.; Wu, M. C.; Chen, C. W.; Su, W. F. Study of the Effect of Annealing Process on the Performance of P3HT/PCBM Photovoltaic Devices Using Scanning-Probe Microscopy. *Sol. Energy Mater. Sol. Cells* **2009,** *93*, 888–892.
19. Campoy-Quiles, M.; Ferenczi, T.; Agostinelli, T.; Etchegoin, P. G.; Kim, Y.; Anthopoulos, T. D.; Stavrinou, P. N.; Bradley, D. D. C.; Nelson, J. Morphology Evolution Via Self-Organization and Lateral and Vertical Diffusion in Polymer: Fullerene Solar Cell Blends. *Nat. Mater.* **2008,** *7*, 158–164.
20. Jo, J.; Na, S. I.; Kim, S. S.; Lee, T. W.; Chung, Y.; Kang, S. J.; Vak, D.; Kim, D. Y. Three-Dimensional Bulk Heterojunction Morphology for Achieving High Internal Quantum Efficiency in Polymer Solar Cells. *Adv. Funct. Mater.* **2009,** *19*, 2398–2406.
21. Germack, D. S.; Chan, C. K.; Hamadani, B. H.; Richter, L. J.; Fischer, D. A.; Gundlach, D. J.; DeLongchamp, D. M. Substrate-Dependent Interface Composition and Charge Transport in Films for Organic Photovoltaics. *Appl. Phys. Lett.* **2009,** *94*, 233303.
22. Yu, B. Y.; Lin, W. C.; Wang, W. B.; Iida, S.; Chen, S. Z.; Liu, C. Y.; Kuo, C. H.; Lee, S. H.; Kao, W. L.; Yen, G. J.; *et al.* Effect of Fabrication Parameters on Three-Dimensional Nanostructures of Bulk Heterojunctions Imaged by High-Resolution Scanning TOF-SIMS. *ACS Nano* **2010,** *4*, 833–840.
23. Parnell, A. J.; Dunbar, A. D. F.; Pearson, A. J.; Staniec, P. A.; Dennison, A. J. C.; Hamamatsu, H.; Skoda, M. W. A.; Lidzey, D. G.; Jones, R. A. L. Depletion of PCBM at the Cathode Interface in P3HT/PCBM Thin Films as Quantified Via Neutron Reflectivity Measurements. *Adv. Mater.* **2010,** *22*, 2444–2447.
24. Samitsu, S.; Shimomura, T.; Heike, S.; Hashizume, T.; Ito, K. Effective Production of Poly(3-Alkylthiophene) Nanofibers by Means of Whisker Method Using Anisole Solvent: Structural, Optical, and Electrical Properties. *Macromolecules* **2008,** *41*, 8000–8010.
25. Merlo, J. A.; Frisbie, C. D. Field Effect Transport and Trapping in Regioregular Polythiophene Nanofibers. *J. Phys. Chem. B* **2004,** *108*, 19169–19179.
26. Nagamatsu, S.; Takashima, W.; Kaneto, K.; Yoshida, Y.; Tanigaki, N.; Yase, K. Backbone Arrangement in "Friction-Transferred" Regioregular Poly(3-Alkylthiophene)s. *Macromolecules* **2003,** *36*, 5252–5257.
27. Yonemura, H.; Yuno, K.; Yamamoto, Y.; Yamada, S.; Fujiwara, Y.; Tanimoto, Y. Orientation of Nanowires Consisting of Poly(3-Hexylthiophene) Using Strong Magnetic Field. *Synth. Met.* **2009,** *159*, 955–960.
28. Qiao, R.; Roberts, A. P.; Mount, A. S.; Klaine, S. J.; Ke, P. C. Translocation of C-60 and Its Derivatives across a Lipid Bilayer. *Nano Lett.* **2007,** *7*, 614–619.
29. Coffey, D. C.; Reid, O. G.; Rodovsky, D. B.; Bartholomew, G. P.; Ginger, D. S. Mapping Local Photocurrents in Polymer/Fullerene Solar Cells with Photoconductive Atomic Force Microscopy. *Nano Lett.* **2007,** *7*, 738–744.
30. Hamadani, B. H.; Jung, S. Y.; Haney, P. M.; Richter, L. J.; Zhitenev, N. B. Origin of Nanoscale Variations in Photoresponse of an Organic Solar Cell. *Nano Lett.* **2010,** *10*, 1611–1617.
31. Pingree, L. S. C.; Reid, O. G.; Ginger, D. S. Imaging the Evolution of Nanoscale Photocurrent Collection and Transport Networks During Annealing of Polythiophene/Fullerene Solar Cells. *Nano Lett.* **2009,** *9*, 2946–2952.
32. Xin, H.; Reid, O. G.; Ren, G. Q.; Kim, F. S.; Ginger, D. S.; Jenekhe, S. A. Polymer Nanowire/Fullerene Bulk Heterojunction Solar Cells: How Nanostructure Determines Photovoltaic Properties. *ACS Nano* **2010,** *4*, 1861–1872.
33. Reid, O. G.; Xin, H.; Jenekhe, S. A.; Ginger, D. S. Nanostructure Determines the Intensity Dependence of Open Circuit Voltage in Plastic Solar Cells. *J. Appl. Phys.* **2010,** *108*, 084320.
34. Wagner, C. D.; Riggs, W. M.; Davis, L. E.; Moulder, J. F.; Muilenberg, G. E. *Handbook of XPS*, 2nd ed.; Physical Electronics: Eden Prairie, MN, 1979.
35. Wenzel, R. N. Resistance of Solid Surfaces to Wetting by Water. *Ind. Eng. Chem.* **1936,** *28*, 988–994.